



OPEN

Integration of frequency selective surfaces with MIMO antennas for enhanced performance in IoT and V2V communication systems

Ikram Troudi¹, Chokri Baccouch²✉, Belgacem Chibani¹, Ahmed Zouinkhi¹, Aymen Flah^{3,4,5,9}, Claude Ziad El-Bayeh⁶, Habib Kraiem⁷ & Monia Oueder⁸

This research explores the integration of Frequency Selective Surfaces (FSS) with Multiple-Input Multiple-Output (MIMO) antennas to enhance communication performance in Internet of Things (IoT) and Vehicle-to-Vehicle (V2V) applications operating at 5.9 GHz. Unlike existing Literature where various FSS structures are employed for performance improvement, this study presents An innovative approach by integrating a decagonal FSS unit cell with a dug-hex microstrip antenna design. The key contributions of this work include significant performance improvements, such as a gain enhancement from 1.46 dB to 6.42 dB for the single-port antenna (32 mm × 24 mm × 1.6 mm), efficiency exceeding 87.45%, And a bandwidth of 738.86 MHz. For the quad-element MIMO antenna (50 mm × 50 mm × 1.6 mm), the FSS integration results in a gain increase from 2.7 dBi to 7.4 dBi across all ports, while also improving frequency selectivity and port isolation. Notably, the MIMO antenna already exhibits good isolation between ports without FSS integration. Experimental validation confirms that the simulated and measured results align closely, demonstrating the effectiveness of the FSS-MIMO integration. This work not only highlights the potential of FSS technology for enhancing antenna performance in IoT and V2V communications but also introduces a novel, compact design that offers significant improvements in gain, efficiency, and bandwidth. The proposed approach is particularly suited for space-constrained environments, providing a valuable contribution to the development of more efficient and robust wireless communication systems, particularly for IoT networks and safer transportation systems.

Keywords Antenna, FSS, MIMO, Fabrication, Bandwidth

The rapid evolution of wireless communication technologies demands continuous advancements in antenna design and signal processing techniques¹.

In addition to the growing need for high-throughput and low-latency communication in IoT and V2V environments, emerging sensing technologies such as LiDAR have revealed the importance of compact, lightweight, and high-precision systems. For instance, the off-axis four-reflection optical structure presented in² enables bathymetric LiDAR systems to achieve accurate depth measurements in aquatic environments using a highly miniaturized 532 nm system mounted on UAVs, with depth errors under 0.1 m And a total volume of 90 × 160 × 90 mm. Similarly, in³, a Lightweight single-band LiDAR on An unmanned shipborne platform addresses topographic survey Limitations in urban and mountainous areas using advanced split-field optics and adaptive signal acquisition, demonstrating depth accuracy better than 30 cm.

¹MACS Laboratory: Modeling, Analysis and Control of Systems LR16ES22 National Engineering School of Gabes, University of Gabes, Gabes, Tunisia. ²Communications Systems LR-99-ES21 National Engineering School of Tunis, LR-Sys'Com-ENIT, University of Tunis, Gabes, Tunisia. ³Jadara University Research Center, Jadara University, Jadara, Jordan. ⁴Applied Science Research Center, Applied Science Private University, Amman 11931, Jordan. ⁵ENET Centre, CEET, VSB-Technical University of Ostrava, Ostrava 708 00, Czech Republic. ⁶Department of Electrical Engineering, Bayeh Institute, Amchit 4307, Lebanon. ⁷Center for Scientific Research and Entrepreneurship, Northern Border University, Arar 73213, Saudi Arabia. ⁸Department of Computer Sciences Applied College, University of Tabuk, Tabuk, Saudi Arabia. ⁹National engineering school of gabes, University of gabes, Gabes, Tunisia. ✉email: chokri.baccouch13@gmail.com

These developments emphasize the convergence of communication and sensing, motivating the integration of intelligent electromagnetic surfaces into antenna systems. Among these, Reconfigurable Intelligent Surfaces (RIS) and Holographic Surfaces (RHS) are increasingly explored for real-time control of wavefronts. In⁴, a comparative study shows that RHS-enabled systems offer superior positioning performance in linear arrays, while RIS performs better in planar arrays with larger surface areas and lower frequencies, illustrating the design tradeoffs for sensing and positioning. In⁵, a robust and adaptive channel estimation method is proposed for IRS-aided mmWave systems, overcoming the challenge of estimating high-dimensional composite channels through compressed-sensing techniques and deep learning frameworks. This is particularly relevant for dense MIMO scenarios at mmWave frequencies, where channel sparsity and passive reflection complicate estimation.

Furthermore, the combination of sensing and communication, referred to as Integrated Sensing and Communication (ISAC), is being actively pursued using hybrid RIS structures. In⁶, a joint beamforming strategy using both active and passive RIS elements is proposed to simultaneously optimize radar sensing and downlink communications in multi-user ISAC systems. These approaches point toward a future where surfaces like FSS, RIS, and RHS play a key role in shaping the radiation characteristics of antennas to meet the dual needs of connectivity and perception.

Multiple-Input Multiple-Output (MIMO) systems have emerged as a key technology in modern wireless communications^{7,8}, offering significant improvements in spectral efficiency and channel capacity⁹. However, with the growing demand for higher data rates and increased reliability, researchers are exploring new approaches to further optimize MIMO system performance¹⁰. This paper investigates the integration of Frequency Selective Surfaces (FSS) with MIMO antennas, a promising approach that leverages the unique electromagnetic properties of FSS to overcome current limitations in MIMO systems^{11,12}.

MIMO technology utilizes multiple antenna elements at both the transmitter and receiver, enabling spatial multiplexing and diversity to enhance channel capacity without requiring additional bandwidth. The integration of FSS, characterized by their frequency-dependent transmission and reflection properties, offers significant potential to manipulate electromagnetic waves and address key challenges in MIMO systems¹³. These challenges include improving isolation between antenna elements, enhancing beam-forming capabilities, extending the operational bandwidth, and more effectively exploiting multipath environments^{14,15}.

FSS can selectively transmit, reflect, or absorb electromagnetic waves at specific frequencies¹⁶. By carefully designing their structure, it is possible to tailor these properties to achieve the desired electromagnetic behavior, which can be exploited to enhance MIMO system performance¹⁷. This selective behavior is key to many of the potential benefits of FSS-MIMO integration¹⁸.

One of the primary challenges in MIMO systems is maintaining sufficient isolation between closely spaced antenna elements to minimize mutual coupling¹⁹. FSS structures address this issue by creating electromagnetic bandgaps or altering the surface current distribution on the antenna substrate. This significantly reduces interference between antenna elements, thereby improving overall system performance²⁰. Another promising aspect of FSS-MIMO integration is its potential to enhance beam-forming capabilities. By designing FSS structures with specific phase responses, it is possible to manipulate the radiation pattern of MIMO antennas, enabling more precise spatial multiplexing²¹. This is particularly beneficial for massive MIMO systems, where the ability to form narrow, high-gain beams is crucial for achieving high spectral efficiency²².

The integration of FSS with MIMO antennas also offers the possibility of extending the operational bandwidth of the system. This is especially valuable in applications requiring broad frequency coverage, such as cognitive radio systems or wideband communication networks. By carefully engineering the FSS response, it is possible to create multi-band or wideband MIMO antennas that maintain high performance over an extended frequency range^{23,24}.

Despite these potential benefits, the integration of FSS with MIMO antennas presents several challenges that require careful consideration. The design of effective FSS structures for MIMO applications demands advanced electromagnetic modeling and optimization techniques²³. Various computational methods are commonly used to analyze and optimize FSS-MIMO systems, each with its strengths and limitations. Furthermore, the performance of FSS is highly sensitive to fabrication accuracy, where even slight deviations from the designed structure can significantly impact their effectiveness.

This study uniquely contributes to understanding the mechanisms of integration, practical implementations, and performance implications of FSS-MIMO systems. Unlike previous research, this work comprehensively examines FSS geometries, adaptive structures, and their applications in addressing critical challenges such as mutual coupling and bandwidth limitations in MIMO systems.

The proposed antenna is particularly suitable for integration into vehicular communication systems, especially those based on Dedicated Short Range Communication (DSRC) protocols operating at 5.9 GHz. Its compact size and enhanced gain make it ideal for mounting on vehicle rooftops or behind bumpers, where low-profile, high-performance antennas are required. This integration supports robust Vehicle-to-Vehicle (V2V) communication by ensuring high directionality and reduced signal loss, even in complex multipath propagation environments.

The remainder of this paper is structured as follows: Sect. 2 discusses the proposed FSS-MIMO design methodology, detailing the principles of electromagnetic modeling and design. Section 3 presents the simulation and experimental results, highlighting the impact of FSS integration on key performance metrics. Finally, Sect. 4 concludes with a summary of the findings and future research directions.

Related work and comparative analysis

Frequency selective surface (FSS)

Recent studies have explored the integration of Frequency Selective Surfaces (FSS) to enhance the performance of MIMO antennas, particularly for sub-6 GHz 5G communications. One such approach is presented in²⁵, where a compact chair-shaped MIMO Antenna with a single-layer FSS structure is proposed. The design utilizes a

parasitic element to improve isolation and an FSS technique to enhance gain. Fabricated on a Rogers 4350B substrate, the Antenna operates between 3 And 6 GHz, achieving a peak gain of 7.96 dBi while maintaining improved isolation. The MIMO performance evaluation through key metrics, including ECC, DG, CCL, MEG, And TARC, confirms its suitability for future 5G systems.

A similar approach is adopted in²⁶, where a millimeter-wave Antenna designed for 5G networks integrates FSS-based reflectors to enhance gain. The rectangular slot Antenna, operating in the fundamental mode of the desired frequency band, sees its gain increase from 4.5 dBi to 10.3 dBi at 28 GHz with the addition of the FSS. Despite a slight reduction in radiation efficiency, the Antenna with FSS maintains a bandwidth from 25.5 GHz to 30.8 GHz with $S11 \leq -10$ dB, confirming its applicability to 5G scenarios.

In²⁷, attention is given to optically transparent MIMO Antennas. The study proposes a design supported by an FSS to enhance gain while maintaining fabrication simplicity. Transparent conductive materials often suffer from reduced conductivity, leading to decreased antenna gain and efficiency. By integrating an FSS beneath the MIMO structure, radiation characteristics are significantly improved. The design, utilizing a Malinex substrate and a silver oxide conductive sheet, achieves an average gain of 4.56 dBi over the 3.09 GHz to 3.7 GHz band while ensuring port isolation greater than 20 dB. This work addresses the challenge of low gain in transparent conductive metal oxide-based antennas.

Another innovative design is presented in²⁸, introducing a low-cost tri-band fractal monopole antenna with a tunable complementary FSS (C-FSS). Fabricated on a 1.6 mm FR-4 substrate, the antenna incorporates an offset feeding technique and a fractal shape to enable dual polarization (linear and circular). With the integration of four PIN diodes for tunability, the design achieves enhanced gain while maintaining its tri-band nature. The measured peak gain at resonating frequencies of 6.0 GHz, 9.05 GHz, And 11.56 GHz reaches 8.24 dBi, 6.04 dBi, And 8.63 dBi, respectively, compared to lower values without the C-FSS. This makes the design suitable for wireless, RADAR, satellite, and microwave applications across C-band, X-band, and additional frequency ranges.

Further advancements in UWB antenna designs are explored in²⁹, where a gain-enhanced UWB antenna is proposed for high-gain wideband communications. Using a coplanar waveguide (CPW) feeding mechanism and a castle-shaped profile, the design extends impedance matching while integrating a Split Center Resonator (SCR) FSS to further enhance gain. Analysis of inter-element spacing and antenna-FSS distance demonstrates a gain improvement of at least 5 dBi, making the design viable for modern UWB communication applications.

For higher-frequency applications³⁰, presents a microstrip-fed printed meandered log-periodic monopole array (PMLPMA) Antenna integrated with an octagonal ring FSS layer. Designed for the 5G n257 (28 GHz) band, the compact antenna system (18.75×18.75 mm 2) consists of five log-periodic monopole elements arranged in two vertically placed PMLPMA units. Simulation results reveal a gain increase from 3.5 dBi to 7.35 dBi with the FSS, as well as An isolation level exceeding 30 dB in the 26.5–29.5 GHz range. Prototype measurements validate the design's potential for 5G mobile applications.

Beyond traditional RF applications³¹, explores a graphene-based THz patch Antenna with an integrated FSS. This design enhances gain from 1.57 dBi to 4.87 dBi while enabling beamforming, multibeam capabilities, And electrostatic tunability over the 0.5–0.65 THz range. These features make it a promising candidate for high-speed THz communication systems.

For X-band applications³², proposes a four-port MIMO Antenna integrating an FSS to enhance gain and reduce mutual coupling. The design achieves a bandwidth of 7.8–9.08 GHz, with a peak gain of 5.2 dBi. The FSS layer ensures stable performance across polarization angles, confirming its efficiency for communication systems.

Finally, in³³, a compact quad-port sub-6 GHz MIMO Antenna with an FSS layer is designed for 5G applications. Covering the 3–5 GHz range, the Antenna exhibits a peak gain improvement from 4 dBi to 7.4 dBi using the FSS. Additionally, it maintains low mutual coupling (< -22 dB) And stable radiation characteristics, making it particularly suitable for 5G MIMO systems.

Through these various studies, it is evident that FSS integration plays a crucial role in enhancing antenna performance across different frequency bands and applications. Whether for sub-6 GHz frequencies, millimeter-wave, or THz frequencies, FSS-based designs consistently demonstrate significant improvements in gain, isolation, and bandwidth, reinforcing their importance in modern wireless communication systems.

These recent works validate the importance of multiband support, pattern diversity, mutual coupling reduction, And conformal integration. Compared to these approaches, the proposed FSS-loaded MIMO antenna introduces a compact and experimentally validated solution operating at 5.9 GHz, offering improved gain, high isolation, and direct integration potential in DSRC-based V2X and compact IoT systems.

Table 1 summarizes recent antenna designs incorporating Frequency Selective Surfaces (FSS) for various applications including 5G, millimeter-wave, and THz bands. The comparison includes key performance metrics such as frequency range, gain, bandwidth, and isolation when available.

MIMO and flexible antenna designs for V2X and IoT systems

Recent research has proposed a variety of advanced antenna designs aimed at improving communication performance in V2X and IoT systems. In³⁴, a flexible and reconfigurable multiband antenna for Vehicle-to-Everything (V2X) communications was developed using PIN diodes directly integrated into the radiating patch. This antenna offers dual-band frequency agility (3.4–3.8 GHz And 5.3–8 GHz), covering key bands such as 5.8 GHz ISM And 5.9 GHz DSRC, while enabling radiation pattern diversity and conformance. Its compact size and low-profile design make it a suitable candidate for wearable and vehicular surfaces.

In³⁵, a 4-port circularly polarized MIMO Antenna operating at 5.9 GHz is presented with a novel hybrid decoupling structure combining parasitic ring elements and a defected ground structure (DGS). This configuration achieves exceptionally high isolation (> 34 dB), a peak gain of 7.68 dBi, low ECC (< 0.001), and

Ref	Antenna type	Frequency (GHz)	Size of antenna (mm)	Size of FSS (mm)	Gain (dB)	Bandwidth (MHz)	MIMO Isolation
²⁵	MIMO with FSS	3.0–6.0	19×43×0.508		7.96	3000	-21 dB
²⁶	Millimeter-wave antenna with FSS	25.5–30.8	12×12×0.203	25×25×5	10.3	5300	--
²⁷	Transparent MIMO antenna with FSS	3.09–3.7	--	--	4.56	610	>20 dB
²⁸	Tunable fractal antenna with C-FSS	6.0, 9.05, 11.56	--	21.13×24.81×1.6	8.24, 6.04, 8.63	--	--
²⁹	UWB antenna with SCR FSS	Wideband	21×21×1.6	21×22.2×1.6	+5.0	6000	--
³⁰	Log-periodic antenna with FSS	26.5–29.5	18.75×18.75×1.55	18.75×18.75×1.55	7.35	3000	>30 dB
³¹	THz patch antenna with FSS	0.5–0.65			4.87	--	--
³²	MIMO antenna with FSS for X-band	7.8–9.08			5.2	--	--
³³	Compact MIMO antenna with FSS	3.0–5.0	45×45×1.6	108×108×1.6	7.4	2000	<-22 dB

Table 1. Comparative results in related works.

Ref	Antenna type	Frequency range (GHz)	Size (mm)	Peak Gain (dBi)	Bandwidth (MHz)	Isolation/ECC	Key features/target application
³⁴	PIN-diode flexible reconfigurable antenna	3.4–3.8 & 5.3–8	0.17λ ₀ ×0.23λ ₀	~7.5	~1800	--	Pattern and frequency reconfigurable V2X antenna
³⁵	4-port CP-MIMO with parasitic & DGS decoupling	5.82–5.94	1.4λ ₀ ×1.4λ ₀	7.68	~120	Isolation>34 dB, ECC<0.001	Long-range V2X, strong diversity
³⁶	Dipole array with radial power divider	27.93–29.13	--	5.42	>1000	--	mmWave IoT sensing, quasi-omnidirectional
³⁷	Conformal 4-port MIMO with circular stubs	5.37–7.34	37×37×0.127	4.63	~1970	ECC<0.005	Wearable & curved IoT/V2X surfaces
³⁸	Stub-loaded compact tri-band monopole	2.35–2.5, 3.3–3.55, 5.18–7.63	--	1.84–2.72	~2200+	--	ISM/5G-IoT tri-band with >75% efficiency
³⁹	12-port integrated microwave/mmWave MIMO	2.37–2.65 to 23–31	--	>6.5 at mmWave	>6000	Isolation>15 dB	360° diversity, indoor & V2×5G
Our work	Decagonal FSS with Dug-Hex Microstrip Antenna	5.9	32×24×1.6 (Single),	5.91–6.42 (Single),	738.86	--	Compact MIMO, V2X/IoT, high isolation and efficiency
			50×50×1.6 (MIMO)	2.7–7.4 (MIMO)		<-30 dB	

Table 2. Summary of recent MIMO, flexible, and V2X/IoT-Specific antenna Designs.

robust diversity performance, demonstrating suitability for long-range V2X links with reliable link budget performance.

Focusing on mmWave IoT sensing³⁶, proposes a quasi-omnidirectional dipole array fed by a radial waveguide power divider, fabricated on Rogers-RO3003C substrate. The Antenna operates between 27.93 And 29.13 GHz with a peak gain of 5.42 dBi And efficiency exceeding 78%. Its modular structure and wide tunable bandwidth (25.56–40.09 GHz) enable it to serve as a robust solution for dense sensor deployment and mmWave IoT access points.

A conformal 4-port MIMO antenna for wireless IoT was developed in³⁷, featuring concentric circular structures And U-shaped stubs for isolation improvement. Operating between 5.37 And 7.34 GHz with a peak gain of 4.63 dBi, the design shows excellent mutual coupling suppression and diversity metrics. Its miniaturized and flexible configuration highlights its application in curved or wearable surfaces for V2X or mobile IoT platforms.

The compact tri-band monopole antenna presented in³⁸ operates across ISM, sub-6 GHz 5G, and IoT bands (2.35–2.5, 3.3–3.55, 5.18–7.63 GHz) with peak gains up to 2.72 dBi. Using slot and stub loading techniques, the antenna achieves wide coverage and omnidirectional performance with radiation efficiency>75%, confirming its viability for multi-standard devices and portable IoT modules.

Finally³⁹, presents An integrated 12-port MIMO Antenna system combining microwave and mmWave elements, enabling 360° pattern diversity for 5G IoT systems. The design supports bands from 2.37 GHz to 31 GHz, with gains over 6.5 dBi at mmWave and >95% radiation efficiency. The antenna demonstrates high isolation and low ECC, supporting seamless connectivity in V2X, indoor environments, and smart infrastructure. Its unique multiband and multi-port architecture makes it the first of its kind offering full coverage from microwave to mmWave with compact integration.

Table 2 presents a comparative overview of recent MIMO, flexible, and reconfigurable antenna designs targeting Vehicle-to-Everything (V2X) and IoT applications. It highlights essential characteristics such as size, frequency bands, isolation, and gain to demonstrate current trends and performance benchmarks.

Compared to the aforementioned studies, the proposed work introduces a compact, experimentally validated decagonal FSS integrated with a Dug-Hex microstrip Antenna, tailored for 5.9 GHz operation in DSRC-based IoT and V2V communications. Unlike previous designs that either target higher frequency bands or involve

complex reconfigurability schemes, our antenna demonstrates a notable gain improvement (from 1.46 dBi to 6.42 dBi for the single-port configuration, And from 2.7 dBi to 7.4 dBi in the MIMO setup), while maintaining low profile and fabrication simplicity. Additionally, the design ensures high radiation efficiency (> 87.45%) and enhanced bandwidth, making it a strong candidate for next-generation vehicular and IoT applications.

Design of a single-port MIMO antenna

Antenna design methodology

The proposed Antenna was designed through a structured approach combining electromagnetic modeling, parametric optimization, and experimental validation. Initially, the antenna geometry was determined based on specific design objectives, including compactness, operating frequency of 5.9 GHz, and high efficiency. The chosen configuration was a novel “dug-hex” microstrip antenna characterized by an octagonal-shaped radiating patch fabricated on an FR4 substrate with dielectric constant (ϵ_r) of 4.3, thickness of 1.6 mm, And loss tangent of 0.025.

The design process began with defining the critical geometric parameters (e.g., patch dimensions, feeding line dimensions, substrate size), detailed in Table 3. Electromagnetic simulations were then conducted using CST Microwave Studio software to optimize these parameters, ensuring optimal impedance matching and radiation characteristics at the target frequency. The reflection coefficient (S_{11}), radiation pattern, gain, and efficiency were iteratively assessed to refine the design.

Following the simulation-based optimization, an equivalent electrical circuit model was developed to accurately characterize the antenna's impedance behavior. This step involved selecting appropriate inductors, capacitors, and resistors to represent resonances, matching conditions, and losses, further aiding in fine-tuning antenna performance.

Finally, the optimized antenna design was fabricated using standard photolithography techniques on an FR4 substrate with copper metallization, ensuring precision and consistency in dimensions. Experimental measurements of the fabricated prototype validated the simulation results, demonstrating a close agreement and confirming the robustness and reliability of the proposed antenna design methodology.

Dug hex antenna design motivation

The design of a compact, efficient antenna is crucial for modern communication systems, especially in applications with limited space, such as Internet of Things (IoT) and Vehicle-to-Vehicle (V2V) communication systems. The “dug hex” antenna, a variation of the microstrip antenna, was chosen for its ability to achieve a balance between compact size, high efficiency, and the desired frequency characteristics.

One of the key challenges in antenna design is ensuring good impedance matching while maintaining a small physical footprint. The hexagonal shape in the “dug hex” design provides a unique geometry that enhances the antenna's ability to operate efficiently at a target frequency while offering robustness against fabrication tolerances. Additionally, the irregular “dug” patch, as opposed to traditional circular or rectangular designs, is known to provide an improved radiation pattern, making it ideal for high-performance applications where space is a constraint, but high efficiency is required. The motivation for this design lies in its ability to meet the stringent size and performance requirements for IoT and V2V communication, particularly in the context of operation at 5.9 GHz.

Dug hex antenna form

Figure 1 presents the design of a dug microstrip antenna, with (a) depicting the front view and (b) the back view. The Antenna is constructed on a rectangular substrate measuring 32 mm (W) by 24 mm (L). The front features an octagonal patch element with radius R , centered on the substrate. A rectangular feed line of width W_f and length L_f extends from the bottom edge towards the patch center. The back view shows a solid rectangular ground plane covering most of the substrate area. This design's key feature is the distinctive octagonal “dug” shape of the

Parameters	Value(mm)
L	30
W	24
Rout1	13
Rin1	12.5
Rout2	4
Rin2	2
W1	3
L1	5
L2	6
Ld	15
Wd	12
H	1.6
T	0.035

Table 3. Parameters of microstrip antenna.

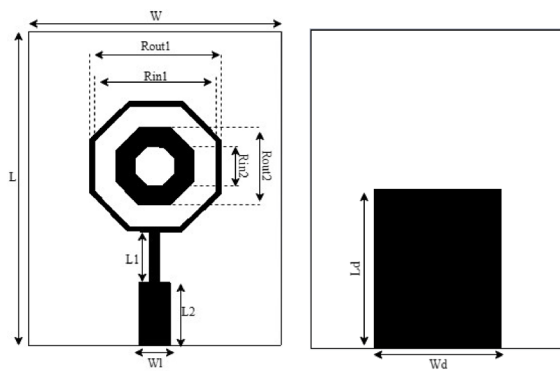


Fig. 1. Design Microstrip Antenna proposed (a) front view (b) back view.

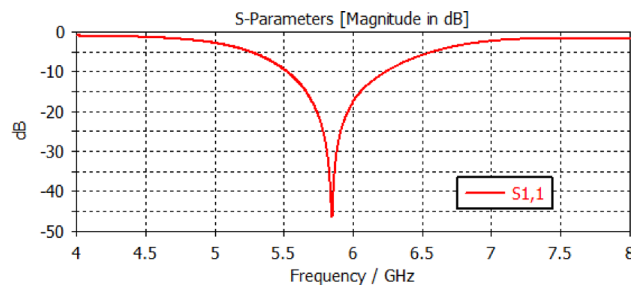


Fig. 2. Reflection Coefficient of proposed microstrip antenna.

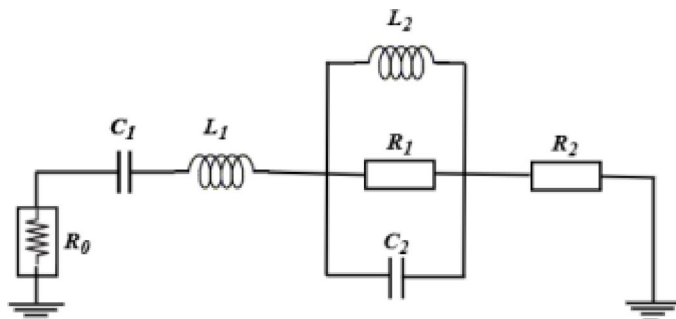


Fig. 3. Equivalent circuit of proposed microstrip antenna.

patch element, which distinguishes it from traditional rectangular microstrip antennas. While specific values for all dimensions are not provided, the figure clearly labels the critical parameters defining this antenna's geometry.

The dimensions of the microstrip antenna proposed are given in Table 3.

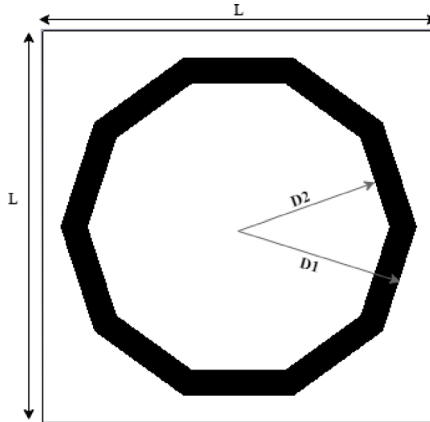
Based on the proposed microstrip antenna, Fig. 2 shows how the reflection parameter S_{11} varies with frequency.

The S_{11} parameter plot in Fig. 2 reveals the frequency response of our proposed dug microstrip Antenna design. We see a pronounced dip in the reflection coefficient at roughly 5.9 GHz, where S_{11} plummets to an impressive -40 dB. This sharp resonance indicates excellent impedance matching at the target frequency, suggesting highly efficient power transfer to the antenna. The bandwidth, while not explicitly marked, appears relatively narrow typical for microstrip designs. This resonance characteristic aligns well with our design goals for operation in the lower C-band. However, we should consider exploring techniques to potentially broaden the bandwidth for more versatile applications. The deep null in S_{11} is particularly noteworthy and warrants further investigation into the specific antenna geometry features contributing to this performance.

Equivalent circuit

The equivalent circuit of the microstrip antenna for V2V communication, illustrated in Fig. 3, models its behavior in terms of impedance, resonance, and losses. It consists of a combination of resistors, inductors, and capacitors, representing the various electrical contributions of the antenna and its environment.

R_0	R_1	R_2	C_1	C_2	L_1	L_2
50 Ohm	0.5 Ohm	50 Ohm	0.04 pF	0.04 pF	18.2 nH	18.2 nH

Table 4. Parameters of equivalent circuit.**Fig. 4.** Proposed FSS.

The circuit input is connected to a resistor, representing the characteristic impedance of the matching system, followed by a network of series and parallel components. A first capacitor is used to isolate DC components and adjust the input impedance. Next, an inductor models the inductive contribution of the antenna's transmission line.

At the center of the circuit, a resistor in series with a parallel network consisting of an inductor and a capacitor represents the resonant behavior of the antenna. This parallel network helps refine the frequency response and improve the antenna's selectivity for better adaptation to V2V communication frequencies.

Finally, a last resistor at the circuit output represents impedance matching and system losses. This model is essential for understanding the antenna's frequency response and optimizing its performance, particularly in terms of reflection, impedance matching, and radiation efficiency.

The values of the different components used in this equivalent circuit—resistances, inductances, and capacitances—are presented in Table 4. These parameters are carefully chosen to reflect the antenna's behavior around its operating frequency, ensuring accurate modeling of its input impedance and resonance characteristics. This model is essential for understanding the antenna's frequency response and optimizing its performance, particularly in terms of reflection, impedance matching, and radiation efficiency.

Design of proposed frequency selective surface (FSS)

The proposed Frequency Selective Surface (FSS) utilizes a decagonal geometry for its unit cell, a distinctive feature that enhances its reflective properties. The goal of designing the FSS is to increase the gain of the MIMO antenna by redirecting electromagnetic waves in a way that creates constructive interference with the primary wave emitted by the antenna. By using this specific geometry, electromagnetic waves incident on the FSS are redirected towards a primary lobe of operation, thus focusing more energy in the desired direction, which increases the gain and directivity of the antenna.

The decagonal unit cell is fabricated on an FR4 substrate, characterized by a dielectric constant of 4.3, a loss tangent of 0.025, And a thickness of 1.6 mm. The critical dimensions of the decagonal unit cell are $D_1 = 6.8$ mm and $D_2 = 5.8$ mm, And the overall unit cell dimensions are 15×15 mm. The reflection And transmission coefficients of the FSS, particularly at the frequency of 5.9 GHz, are key to enhancing antenna performance, as shown in Fig. 4.

The high transmission coefficient of the FSS at 5.9 GHz enables efficient interaction of electromagnetic waves with the FSS, which redirects downward waves back towards the antenna. This reflected wave constructively interferes with the primary wave emitted by the antenna, resulting in enhanced gain and directivity. The careful placement of the FSS at a distance corresponding to λ (the wavelength) ensures optimal phase alignment, further maximizing this constructive interference and optimizing the overall radiation pattern.

By integrating this FSS behind the antenna, we leverage this constructive interference to increase the radiated energy in the desired direction, while minimizing losses and improving the overall system performance, particularly in terms of gain and directivity.

This design underscores the FSS's potential for effective manipulation of electromagnetic waves. The FSS's ability to achieve desired reflection and transmission characteristics makes it a promising component in various applications requiring frequency-selective filtering or wave redirection.

The performance of the proposed FSS is illustrated in Fig. 5, which presents the simulated S-parameters. The reflection coefficient (S_{11}) remains low across the frequency band, while the transmission coefficient (S_{21})

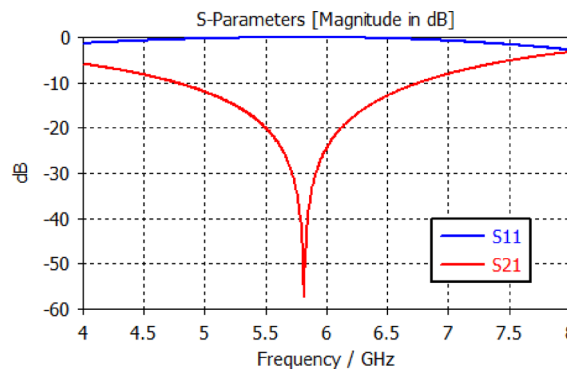


Fig. 5. Reflection Coefficient S11 and transmission coefficient S21 of FSS.

Distance (mm)	Normalized Distance (λ)	S11 (dB)	Gain (dBi)
12.7	0.25 λ	-22.00	6.45
25.4	0.50 λ	-23.00	4.79
38.1	0.75 λ	-25.00	7.49
50.8	1.00 λ	-25.00	3.85

Table 5. Effect of antenna-to-FSS distance on s11 and gain at 5.9 GHz.

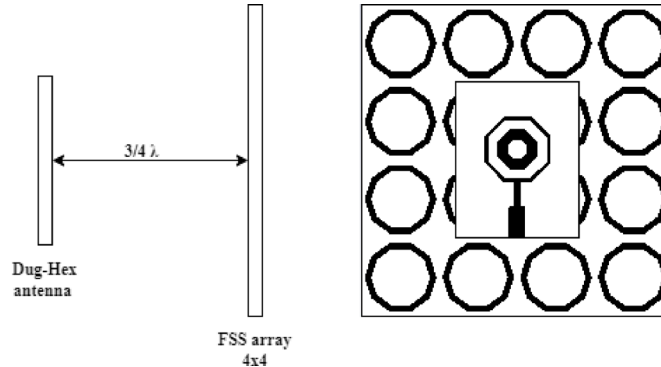


Fig. 6. Side profile of Dug-Hex antenna with FSS reflector.

shows a sharp resonance around 5.9 GHz, indicating strong frequency selectivity and minimal insertion loss at the target frequency. This confirms the FSS's effectiveness in isolating and transmitting specific frequency bands, particularly relevant in applications such as V2V communication and electromagnetic shielding.

The FSS is configured as a 4×4 array of unit cells. Each unit cell has dimensions of $60 \text{ mm} \times 60 \text{ mm}$ And a periodicity of 2 mm. The dimensions of the individual cells are consistent with the overall dimensions of the array.

Single-port MIMO antenna with Fss Results and discussion

To assess the impact of the Antenna-to-FSS distance on performance, a parametric study was conducted where the separation was varied from 0.25λ to λ ($\lambda = 50.8 \text{ mm}$ at 5.9 GHz). For each configuration, the reflection coefficient (S11) and gain were extracted. This evaluation helps to identify the optimal distance that maximizes constructive interference between the direct and reflected waves. Table 5 summarizes the measured S11 and gain values for the different separation distances.

As shown in Table 5, the best performance in terms of gain is achieved when the antenna is placed at a distance of $\frac{3}{4}\lambda$, reaching a gain of 7.49 dBi and a deep reflection coefficient of -25 dB . While the configuration at 1.0λ also exhibits low S11, the gain drops significantly, likely due to destructive interference effects or phase misalignment. The results confirm that a proper alignment between the direct and reflected waves is essential to enhance the gain via constructive interference. These findings are consistent with prior studies on FSS reflectors, and they validate the importance of tuning the antenna-FSS spacing to maximize radiation efficiency.

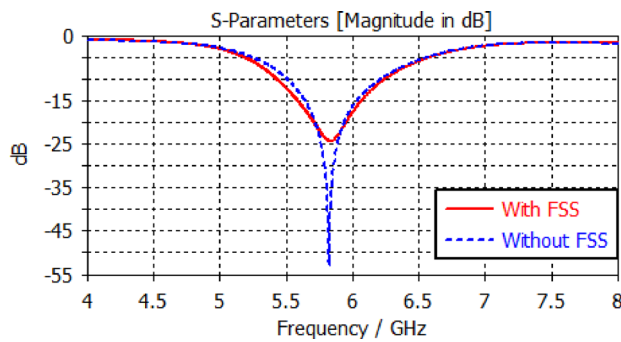


Fig. 7. Reflection coefficients of patch antenna without and with FSS reflector.

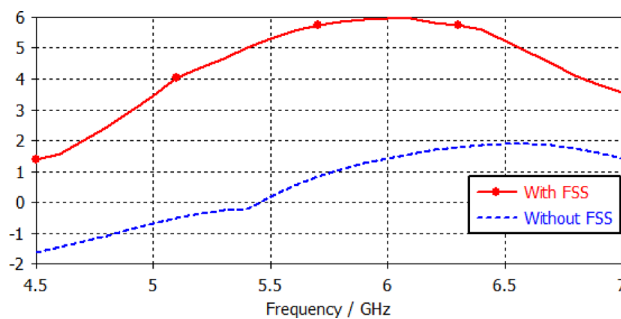


Fig. 8. Antenna gain evaluation: impact of FSS reflector.

The antenna emits a wave that propagates both upward from the patch and downward through the partial ground plane. By incorporating an FSS reflector at a distance of λ from the antenna, the downward wave is redirected back towards the antenna, effectively creating a secondary source of emission. This secondary wave undergoes reflection and travels a distance of λ before interfering with the primary wave emitted from the patch. Due to the phase alignment of these waves, constructive interference occurs, leading to a modified radiation pattern. The resulting antenna exhibits omnidirectional radiation above the patch, enhancing its directivity and gain.

When integrated into an electronic circuit, the antenna serves as an effective electromagnetic shield for the ground plane, further contributing to its functionality in IoT communication applications.

The presence of the FSS significantly impacts the antenna's reflection coefficient (S11), as depicted in Fig. 7. The graph illustrates a notable reduction in the input reflection coefficient value from -46.34 dB to -25.16 dB at a frequency of 5.9 GHz. Moreover, the antenna's -10 dB bandwidth, centered at 5.9 GHz, is measured to be 738.86 MHz. This narrower bandwidth is particularly beneficial for Vehicle-to-Vehicle (V2V) communication within the Dedicated Short Range Communication (DSRC) system frequency. The comparison between the scenarios with and without FSS highlights the antenna's improved performance at 5.9 GHz, a critical factor for efficient V2V communication.

Figure 8 compares the performance of the antenna with and without an FSS reflector. The reflector significantly enhances the antenna's gain, increasing from 1.46 dB to 6.42 dB at a frequency of 5.9 GHz. This gain enhancement is achieved while maintaining the other antenna characteristics.

Figure 9 demonstrates the notable efficiency enhancement of the Antenna when combined with an FSS. This integration enables the antenna to operate within its intended frequency range with an efficiency exceeding 87.45% .

Effect of FSS on antenna characteristics

These results are consistent with prior research demonstrating the benefits of FSS integration. For instance, in a CPW-fed UWB Antenna loaded with a single-layer FSS achieved a bandwidth increase from 5 to 17 GHz to 3 – 18 GHz And a gain enhancement from 6.5 dBi to 10.5 dBi. Similarly, in⁴⁰, the addition of An FSS reflector to a miniaturized monopole antenna resulted in at least 4 dBi gain improvement across the entire operating band. In⁴¹, the use of a flexible RIS layer enabled pattern reconfigurability And boosted gain from 3.4 to 7.93 dBi. Additionally, a tri-band fractal antenna with tunable C-FSS reported in²⁸ showed up to 1.5 dBi gain enhancement at each band of interest. These studies collectively support the effectiveness of FSS loading, And the observed performance improvements in our proposed antenna, specifically a gain enhancement of 6.42 dB And efficiency exceeding 87% validate the design approach and confirm its suitability for high-performance wireless applications.

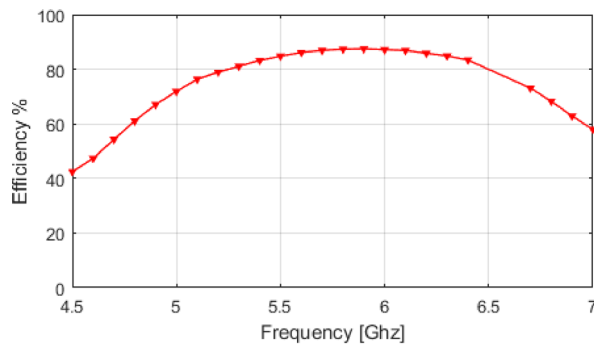


Fig. 9. Efficiency of patch antenna versus frequency with FSS.

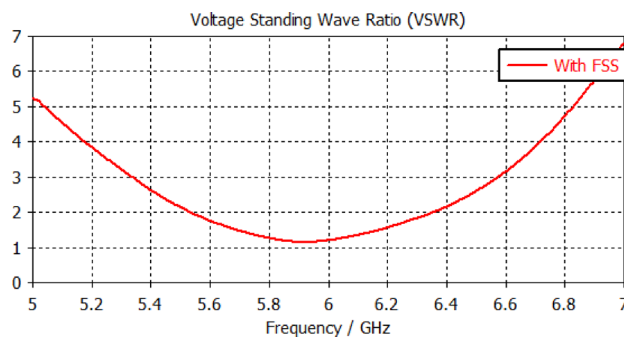


Fig. 10. Voltage Standing Wave Ratio (VSWR) for patch antenna with FSS.

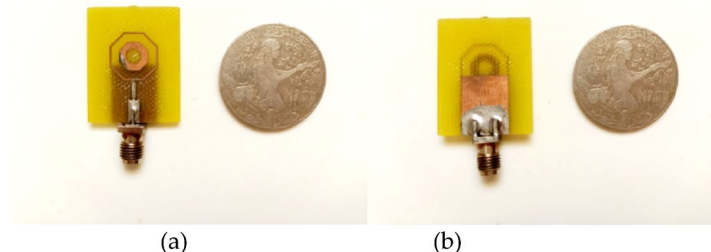


Fig. 11. Fabricated Design Dug-Hex antenna proposed (a) front view (b) back view.

The Voltage Standing Wave Ratio (VSWR) of the FSS-equipped patch antenna, as shown in Fig. 10, is measured to be 1.17 at 5.9 GHz. This value, below the VSWR threshold of 2, indicates a favorable impedance match between the feed line and the antenna. Such a well-matched impedance ensures efficient power transfer, leading to improved overall antenna performance.

Validation results

To experimentally validate the proposed Dug-hex antenna and FSS, a fabrication process was conducted in a fab lab, as depicted in Figs. 11 and 12. The fabrication adhered to the parameters outlined in the previous table, utilizing FR4 for the substrate and copper for the antenna. The subsequent sections offer a detailed comparative analysis between the simulated and measured results.

Figure 13 illustrates that there is no substantial difference between the measured and simulated S-parameters for both configurations, with and without the FSS. The close agreement between the two sets of results suggests that the experimental data aligns well with the theoretical predictions. This confirms the accuracy of the design and fabrication process, validating the performance of the proposed Dug-hex antenna and FSS.

Analysis of quad-element mimo antenna results

A quad-element Multiple-Input Multiple-Output (MIMO) Antenna was designed by arranging the individual antenna units in an orthogonal configuration. The MIMO system has specific dimensions of 50 mm × 50 mm ×

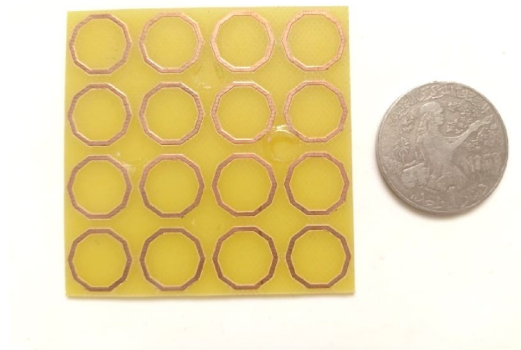


Fig. 12. Fabricated Design of proposed FSS.

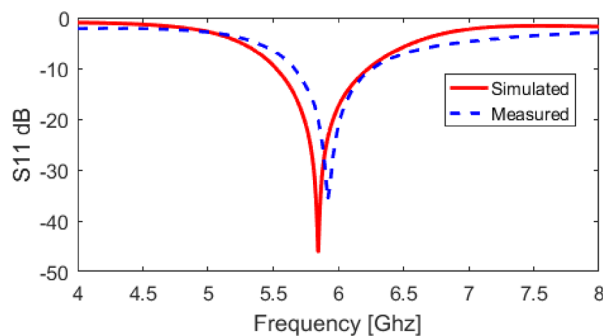


Fig. 13. Measured and simulated S-Parameter results of antenna without FSS and with FSS.

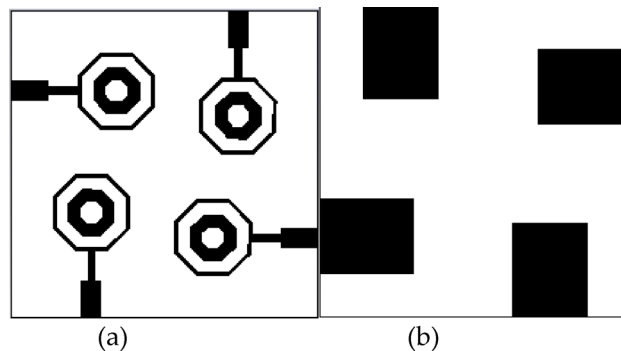


Fig. 14. Bottom and Ground view of proposed MIMO Antenna.

1.6 mm. Figure 14 illustrates the bottom schematic view of the MIMO antenna in part (a) and the ground plane in part (b), respectively.

As depicted in Fig. 15, the S11 parameters of the MIMO antenna, obtained from four ports (two inputs and two outputs), indicate a value below -10 dB, which is generally considered indicative of good impedance matching in Antenna design. This favorable matching is observed at a frequency of 5.9 GHz with An approximate bandwidth of 755.58 MHz.

Results and discussions

Figure 16 shows a Frequency Selective Surface (FSS) array positioned behind a MIMO Antenna. The FSS array consists of a 4×4 arrangement of unit cells, with optimal antenna reflection achieved when the separation distance between the antenna and the FSS is set to $\frac{3}{4} \lambda$, where λ represents the wavelength corresponding to the resonant frequency of 5.9 GHz.

The antenna generates a wave that propagates upwards from the patch and downwards through the partial ground plane. By introducing a reflector consisting of FSS cells positioned at a distance of λ from the antenna,

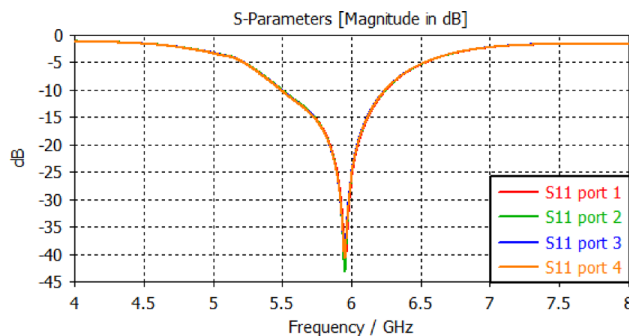


Fig. 15. Reflection coefficient of MIMO Antenna.

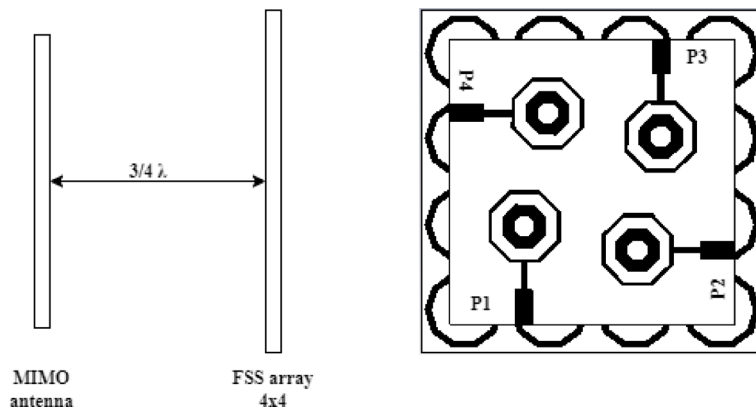


Fig. 16. Side Profile of MIMO Antenna with FSS Reflector.

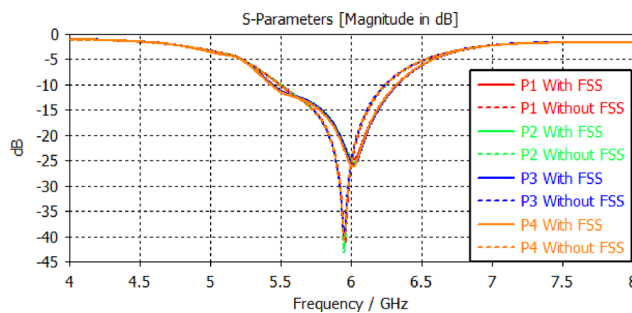


Fig. 17. S11 with and without FSS for Four port.

the downward-propagating wave is redirected back towards the antenna, effectively functioning as an additional source of emission. As a result, the antenna combines two waves: the primary wave originating from the patch and the secondary wave from the reflector. The secondary wave, having been reflected, travels a distance of λ before interacting with the primary wave. This interaction leads to constructive interference, as the waves are in phase, thereby altering the radiation pattern. Consequently, the antenna exhibits omnidirectional radiation above the patch, enhancing both its directivity and gain.

Moreover, when integrated into an electronic circuit, the antenna acts as an effective electromagnetic shield for the ground plane. This integration further enhances the antenna's functionality, particularly in facilitating IoT communication.

Figure 17 shows the S11 parameter results for the four ports of the MIMO Antenna, both with and without the FSS reflector. The results highlight a primary resonance around 6 GHz, which aligns with the system's target operating frequency, confirming that the design is on track. The effect of the FSS reflector is noticeable, as the solid lines (with FSS) display deeper dips compared to the dashed lines (without FSS), which indicates improved wave reflection and reduced losses. The FSS reflector also enhances impedance matching, particularly around 6 GHz, with S11 values dropping below -10 dB. This translates to better radiation efficiency and improved

overall antenna performance. When comparing this to the previous figure, which shows the MIMO antenna and FSS array configuration, it's clear that positioning the FSS at a distance of $\frac{3}{4}\lambda$ from the antenna plays a key role in these performance gains. The FSS effectively reflects the waves back toward the antenna, creating constructive interference, which not only alters the radiation pattern but also boosts both directivity and gain.

Figure 18 presents the far-field E-field radiation patterns at 5.9 GHz for the four antenna ports (P1, P2, P3, and P4), measured at two different azimuthal angles: $\Phi = 0^\circ$ and $\Phi = 90^\circ$. The polar plots illustrate the variation of the electric field intensity in terms of θ around the antenna, with each color representing one of the four ports.

At $\Phi = 0^\circ$, the radiation patterns show a characteristic multi-lobe structure for each port. This lobed pattern indicates that the antenna radiates in several distinct directions with varying intensities. The different lobes correspond to the directions where the antenna has maximum radiation, while nulls (or minimal) occur in directions where radiation is weak or nonexistent. Despite some slight differences in lobe amplitude between the four ports, the overall patterns are quite symmetrical, demonstrating balanced radiation characteristics across all ports.

Similarly, at $\Phi = 90^\circ$, the patterns maintain a multi-lobe structure but with a different orientation compared to $\Phi = 0^\circ$. The shape of the lobes is slightly altered, showing that the antenna's radiation varies depending on the azimuthal plane. However, the overall structure remains consistent, reflecting the antenna's stable performance in different planes. The symmetry and uniformity of these lobes are crucial for applications where the antenna needs to cover a wide range of directions, such as MIMO and IoT systems.

The presence of multiple lobes in both $\Phi = 0^\circ$ and $\Phi = 90^\circ$ planes demonstrates that the antenna is capable of providing extensive directional coverage, which is essential for ensuring reliable communication. The minor variations in the radiation pattern across different ports might be attributed to slight asymmetries in the antenna design or fabrication, but these variations do not significantly impact the overall radiation performance. The patterns also suggest that the antenna offers good omnidirectional coverage, which is critical for MIMO systems where signals must be transmitted and received from multiple directions simultaneously.

In summary, the radiation patterns in Fig. 18 confirm that the Antenna achieves robust and stable multidirectional radiation at 5.9 GHz, making it well-suited for applications requiring extensive spatial coverage and high directivity, such as MIMO and IoT systems. The consistency in performance across the four ports further underscores the antenna's effectiveness in such scenarios.

Figure 19 illustrates the far-field H-field radiation patterns at 5.9 GHz for four antenna ports (P1, P2, P3, and P4) at two azimuthal angles: $\Phi = 0^\circ$ and $\Phi = 90^\circ$. Similar to the E-field patterns in Fig. 17, these H-field patterns show a multi-lobe structure, indicating directions of maximum radiation. The patterns at $\Phi = 0^\circ$ are rounded and balanced across ports, while those at $\Phi = 90^\circ$ exhibit a consistent orientation shift. This stability in both planes confirms the antenna's suitability for applications like MIMO and IoT systems that require extensive and reliable directional coverage.

Figure 20 shows the 3D radiation patterns of the MIMO antenna with a frequency-selective surface (FSS). The four subfigures (a), (b), (c), and (d) represent the radiation patterns for the four Antenna ports. Each diagram illustrates the 3D gain distribution, highlighting the regions of maximum and minimum radiation around the antenna.

The patterns reveal a degree of uniformity in the radiation distribution across the ports. However, each port exhibits slightly different distributions due to the antenna configuration and interactions with the FSS. This relative consistency in gain and spatial coverage confirms the MIMO antenna with FSS's ability to provide effective multidirectional coverage, which is crucial for communication systems that require high reliability and omnidirectional coverage.

Figure 21 highlights the significant impact of the frequency-selective surface (FSS) on the MIMO antenna's performance at 5.9 GHz. Without the FSS, the Antenna exhibits a consistent gain of around 2.7 dBi for all ports (P1, P2, P3, and P4). However, with the FSS, the gain improves dramatically, reaching values between 7.1 And 7.4 dBi. This demonstrates a gain increase of nearly 4.5 dBi, confirming the FSS's critical role in enhancing the antenna's performance, making it more suitable for high-efficiency applications such as MIMO systems.

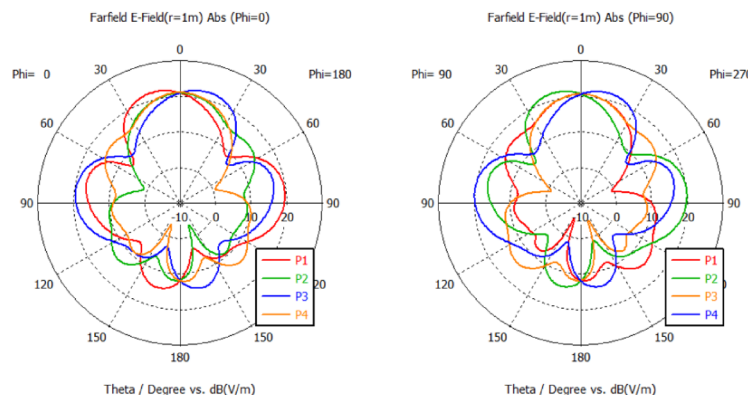


Fig. 18. FarFiled E-Filed for 5.9 GHz at $\Phi = 0^\circ$ and at $\Phi = 90^\circ$.

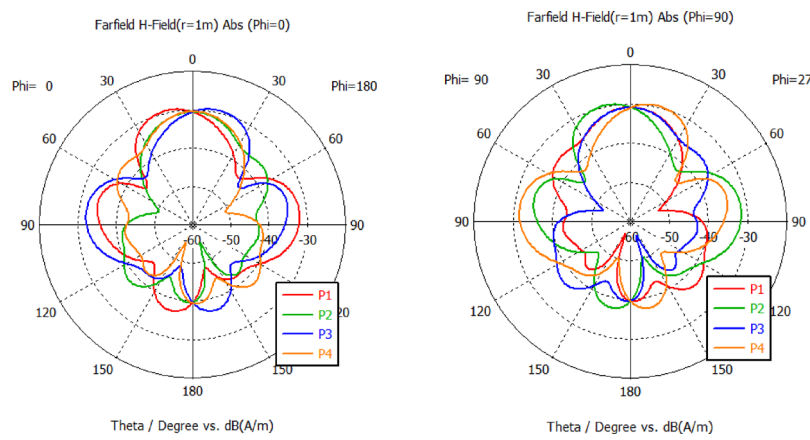


Fig. 19. FarField H-Field for 5.9 GHz at $\Phi=0^\circ$ and at $\Phi=90^\circ$.

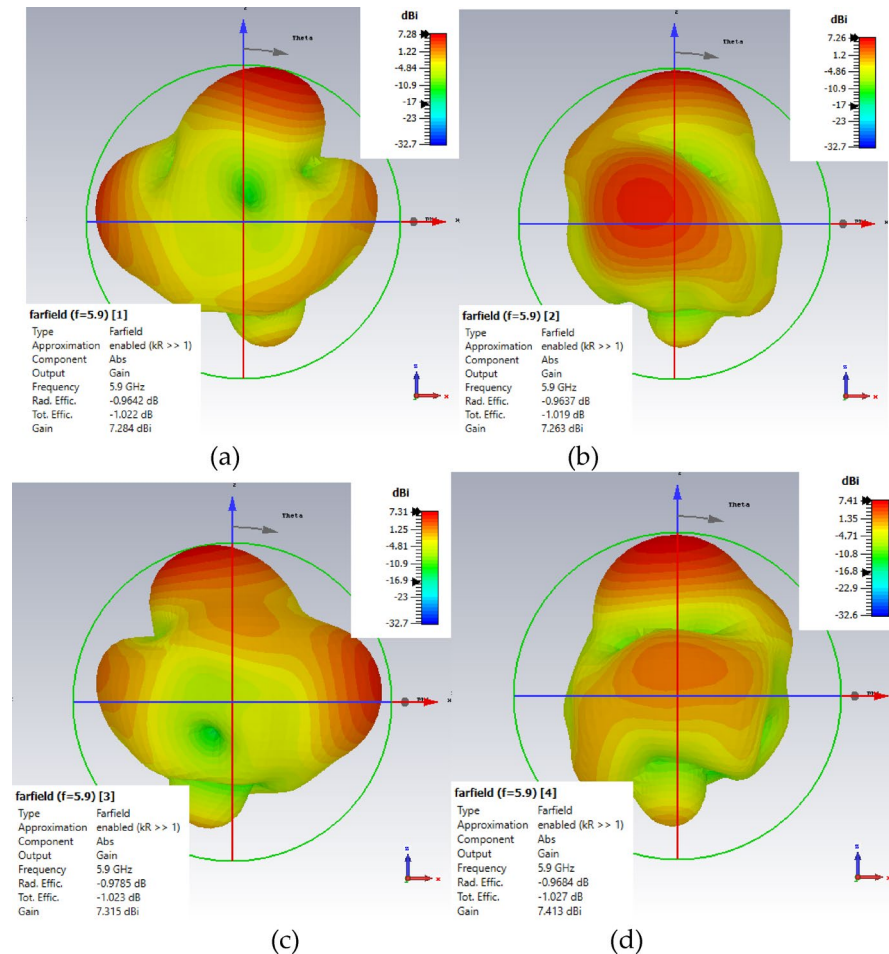


Fig. 20. 3D radiation pattern of MIMO Antenna with FSS.

Validation results

In this Fig. 22, a fabricated design of a MIMO antenna is presented as part of the validation process. The photograph shows the physical implementation of the antenna on a substrate, with distinct ports (labeled P1, P2, P3, and P4) which correspond to different feeding points, possibly for multi-input multi-output functionality. The MIMO antenna appears to be constructed using a PCB (printed circuit board) with connectors to allow for signal feeding.

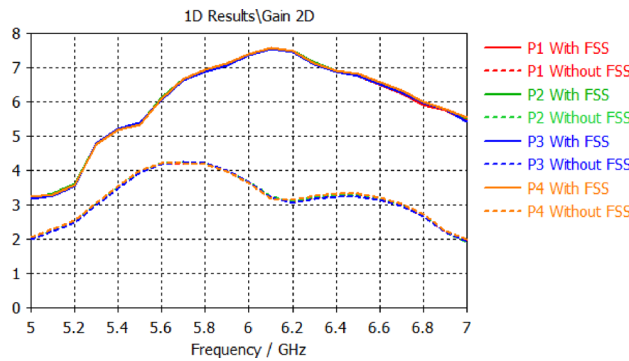


Fig. 21. MIMO Antenna Gain Evaluation: Impact of FSS.

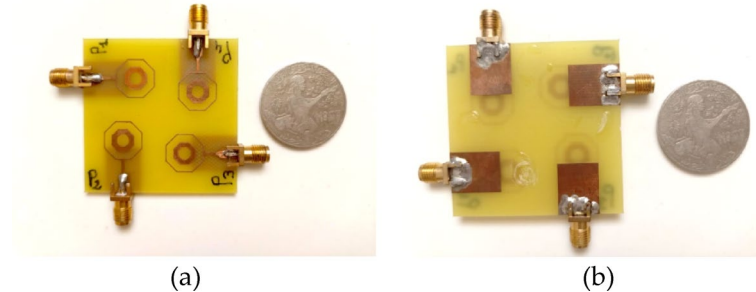


Fig. 22. Fabricated Design MIMO Antenna proposed (a) front view (b) back view.

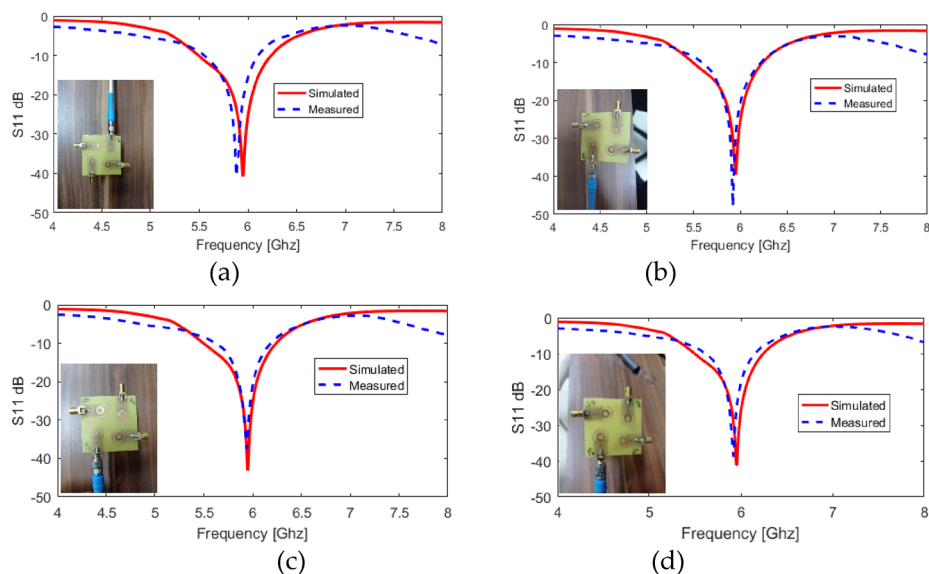


Fig. 23. Validation MIMO Antenna without FSS (a) Port 1 (b) Port 2 (c) Port 3 (d) Port 4.

This fabricated prototype is essential for validating the simulation or theoretical models, as physical testing allows for performance evaluation in real-world conditions, such as measuring return loss, gain, and radiation pattern. The quality of the soldering, as seen in the image, ensures proper electrical connectivity and minimizes interference, which is critical for the accuracy of the results.

By showcasing both the front and back of the antenna, the figure provides a complete view of the proposed design's physical structure, which reinforces the practical applicability of the antenna in actual use cases.

In Fig. 23 above, the validation of a MIMO antenna without Frequency Selective Surface (FSS) is presented by comparing simulated and measured S11 (return loss) parameters for four different ports. The results span a

frequency range from 4.5 GHz to 8 GHz, with the red curves representing simulated data and the blue dashed curves representing measured data. Both curves show a good agreement, with a resonance frequency around 5.5 GHz. At this frequency, the return loss drops below -10 dB for all ports, indicating effective impedance matching and good radiation performance. While minor variations are observed between ports, the overall performance is consistent, demonstrating stable and uniform behavior of the MIMO system without FSS. This alignment between the simulated and measured results validates the antenna design and its performance in the absence of FSS.

In contrast, Fig. 23 below illustrates the validation of the same MIMO antenna system, this time with the integration of a Frequency Selective Surface (FSS). The S11 results, both simulated and measured, are again compared for the four ports, and the frequency range remains the same. However, the inclusion of the FSS causes a slight shift in the resonance frequency to around 5.6 GHz. Additionally, the return loss drops more sharply below -10 dB at this frequency, indicating improved impedance matching and better antenna selectivity. The FSS also enhances the frequency response by creating more pronounced dips in return loss, leading to better frequency filtering and increased isolation between the MIMO ports. Despite minor discrepancies in the measured data, the overall performance remains uniform across the four ports, confirming the positive impact of FSS on optimizing the antenna's performance.

In summary, Fig. 23 shows that the MIMO antenna without FSS already provides satisfactory performance, with good alignment between simulated and measured data, while Fig. 24 demonstrates that the addition of an FSS improves the resonance characteristics by slightly shifting the frequency and enhancing both return loss and system consistency across the ports. These results validate the effectiveness of FSS in optimizing the MIMO antenna design and performance.

Figure 25 presents the coupling transmission results S21 between different port pairs in the MIMO system without the integration of the Frequency Selective Surface (FSS). The results show that, while isolation between the ports is acceptable, some mutual coupling remains, especially between ports 23 and 34, where coupling values exceed -15 dB at 5.9 GHz. This indicates moderate interference between these ports, likely due to their proximity and electromagnetic coupling.

On the other hand, ports 12 and 41 exhibit lower coupling, which could be advantageous in applications where weaker coupling is desirable. While the isolation without FSS is sufficient for many applications, there is still potential for improvement.

Although the results without FSS are satisfactory, integrating the FSS is expected to further enhance port isolation by reducing mutual coupling through the creation of an electromagnetic bandgap and redistribution of surface currents. This should particularly improve the coupling observed between more sensitive ports, such as 23 and 34, and maintain low coupling where required, like between ports 12 and 41.

5.3. Link Budget Consideration for V2X and IoT Scenarios.

To assess the applicability of the proposed antenna in practical V2X communication scenarios, a link budget evaluation was performed for a typical line-of-sight (LOS) scenario between two vehicles separated by 300 m operating at 5.9 GHz. Using the Friis transmission equation:

$$P_r = P_t + G_t + G_r - 20\log_{10}(f) - 20\log_{10}(d) - 32.45$$

where $P_t = 20$ dBm (transmit power), $G_t = G_r = 7.4$ dBi (measured antenna gain), $f = 5.9$ GHz, and $d = 300$ m. The received power is:

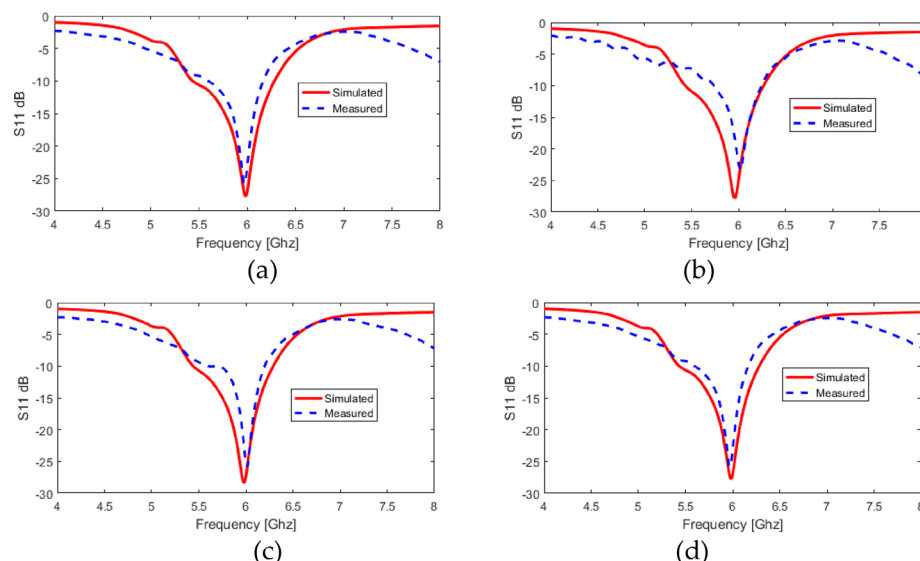


Fig. 24. Validation MIMO Antenna with FSS **(a)** Port 1 **(b)** Port 2 **(c)** Port 3 **(d)** Port 4.

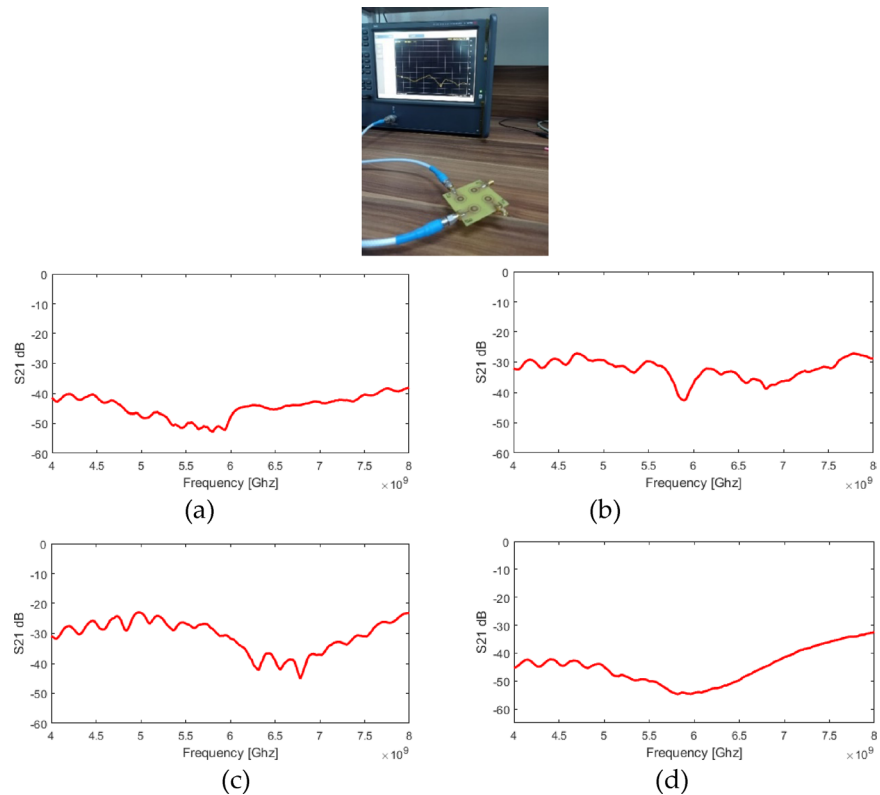


Fig. 25. Coupling Transmission (a) Ports 12 (b) Ports 23 (c) Port 34 (d) Port 41.

$$P_r \approx -22.55 \text{ dBm}$$

This value is significantly higher than the DSRC receiver sensitivity threshold (typically -85 dBm), confirming that the proposed antenna ensures robust and reliable communication over practical V2V distances. This result supports the system design principles discussed in⁴⁰, which emphasizes link margin as a critical parameter in V2X systems.

Conclusions

In this paper, we have demonstrated the successful integration of Frequency Selective Surfaces (FSS) with Multiple-Input Multiple-Output (MIMO) antennas for IoT and Vehicle-to-Vehicle (V2V) communication systems operating at 5.9 GHz. The study focused on a novel dug-hex microstrip Antenna design and a decagonal FSS unit cell. For the single-port antenna, the FSS integration resulted in significant improvements, including a gain enhancement from 1.46 dB to 6.42 dB, efficiency exceeding 87.45%, And a bandwidth of 738.86 MHz. The quad-element MIMO Antenna similarly benefited, with gain improving from 2.7 dBi to 7.4 dBi across all ports, along with enhanced frequency selectivity and port isolation.

Importantly, we validated these results through fabrication and measurement of both the single-port and MIMO antennas, as well as the FSS structure. The experimental validation confirmed close agreement between simulated and measured results, demonstrating the effectiveness of the FSS-MIMO integration approach. The fabricated prototypes exhibited performance characteristics closely matching the theoretical predictions, further reinforcing the reliability and practical applicability of our design.

These findings underscore the promising potential of FSS technology in enhancing antenna performance for IoT and V2V applications, contributing to the development of more efficient wireless communication systems. The compact design coupled with improved gain, efficiency, and bandwidth makes this approach particularly suitable for applications where space is limited, potentially leading to improved IoT networks and safer transportation systems. The successful fabrication and validation of the proposed designs pave the way for real-world implementation of these enhanced antenna systems in future IoT and V2V communication platforms.

Data availability

The datasets used during the current study are available from the first author on reasonable request.

Received: 29 January 2025; Accepted: 9 September 2025

Published online: 10 October 2025

References

- Murasing, F. H. & ADVANCEMENTS IN ANTENNA ARRAY DESIGN FOR 5G COMMUNICATION NETWORKS. A COMPREHENSIVE REVIEW. *Int. J. Sci. Res. Mod. Sci. Technol.* **3**(2), 01–14 (2024).
- Li, Y., Liu, Y., Tang, X., Zhang, C. & Li, Y. Off-Axis Four-Reflection optical structure for lightweight Single-Band bathymetric lidar. *Remote Sens.* **15**, 3945 (2023).
- Zhou G., Zhou X., Li W., Zhao D., Song B., Xu C., et al. Development of a lightweight single-band bathymetric LiDAR. *Remote Sensing* **14**, 5880. <https://doi.org/10.3390/rs14225880> (2022)
- Zhou, Y., Yuan, Y., Shi, Y., Wang, Y. & Zhang, Y. Target detection and positioning aided by reconfigurable surfaces: reflective or holographic?? *IEEE Trans. Signal Process.* **71**, 3156–3171 (2023).
- Chu S., Pan C., Jiang S., Li J., Zheng C. Adaptive and robust channel estimation for IRS-aided millimeter-wave communications. *IEEE Trans Veh Technol.* **73**(7), 9411–9423. <https://doi.org/10.1109/TVT.2024.3385776> (2024).
- Fang, Q., Zhang, Y. & Ma, X. Joint active and passive beamforming design for hybrid RIS-Aided integrated sensing and communication. *IEEE Trans. Commun.* **71**, 4152–4166. <https://doi.org/10.1109/TCOMM.2023.3280427> (2023).
- Wu, Y. et al. A survey on MIMO transmission with finite input signals: Technical challenges, advances, and future trends. *Proceedings of the IEEE* **106**(10), 1779–1833 (2018).
- Huo Y. et al. Technology trends for massive MIMO towards 6G. *Sensors.* **23**(13), 6062. <https://doi.org/10.3390/s23136062> (2023)
- Iyer, S. et al. A survey on technological trends to enhance spectrum-efficiency in 6 g communications. *Trans. Indian Natl. Acad. Eng.* **7** (4), 1093–1120 (2022).
- Ahmad, I. et al. Latest performance improvement strategies and techniques used in 5G antenna designing technology, a comprehensive study. *Micromachines* **13** (5), 717 (2022).
- Ullah H., Cao Q., Khan I., Rahman SU., Jabire AH. A novel frequency selective surface loaded MIMO antenna with low mutual coupling and enhanced gain. *Prog Electromagn Res M.* **118**, 83–92. <https://doi.org/10.2528/PIERM23040607> (2023).
- Ramos A., Varum T., Matos JN. A review on mutual coupling reduction techniques in mmWaves structures and massive MIMO arrays. *IEEE Access.* <https://doi.org/10.1109/ACCESS.2023.3343107> (2023).
- Di Renzo et al. Spatial modulation for generalized MIMO: Challenges, opportunities, and implementation. *Proceedings of the IEEE* **102**(1), 56–103 (2013).
- Plapous C., Marro C., Scalart P. Improved signal-to-noise ratio estimation for speech enhancement. *IEEE Trans Audio Speech Lang Process.* **14**(6), 2098–2108. <https://doi.org/10.1109/TASL.2006.872621> (2006).
- Jamshidi-Zarmehri, H. et al. A review on through-wall communications: wall characterization, applications, technologies, and prospects. *IEEE Access.* **11**, 127837–127854 (2023).
- Raj T. et al. Advances in MIMO antenna design for 5G: a comprehensive review. *Sensors.* **23**(14), 6329. <https://doi.org/10.3390/s23146329> (2023).
- Sayed, A. M. & Raghavan, V. Maximizing MIMO capacity in sparse multipath with reconfigurable antenna arrays. *IEEE J. Selc. Topics Signal Process.* **1** (1), 156–166 (2007).
- Zerrad, F. E. & Taouzari, M. Frequency Selective Surfaces (FSSs) in Metamaterials. *Advanced Metamaterials for Engineers* 6–1 (IOP Publishing, 2023).
- Sharma U. et al. Design challenges and solutions of multiband MIMO antenna for 5G/6G wireless applications: a comprehensive review. *Prog Electromagn Res B.* **104**. <https://doi.org/10.2528/PIERB23101904> (2024).
- Desai, A. et al. FSS based high gain optically transparent MIMO antenna for Sub-6 ghz 5G mid-band applications. *Optik* **307**, 171829 (2024).
- Zhu, S. H. et al. Mutual coupling reduction of $\pm 45^\circ$ dual-polarized closely spaced MIMO antenna by topology optimization. *IEEE Access.* **8**, 29089–29098 (2020).
- Singh, A., Kumar, A. & Binod Kumar Kanaujia. High gain and enhanced isolation MIMO antenna with FSS and metasurface. *Optik* **286**, 170982 (2023).
- Elalaouy, O., Ghzaoui, M. E. & Foshi, J. Mutual coupling reduction of a two-port MIMO antenna using defected ground structure. e-Prime-Advances in electrical engineering. *Electron. Energy.* **8**, 100557 (2024).
- Abdelfatah M., Zekry A., ElSayed S. Orthogonal beamforming technique for massive MIMO systems. *Ann Telecommun.* **80**(1), 79–97. <https://doi.org/10.1007/s12243-024-01013-9> (2025).
- Zeain MY. et al. A new technique of FSS-based novel chair-shaped compact MIMO antenna to enhance the gain for Sub-6 GHz 5G applications. *IEEE Access.* **12**, 49489–49507. <https://doi.org/10.1109/ACCESS.2024.3380013> (2024).
- Amraoui, Y. et al. High gain MIMO antenna with multiband characterization for Terahertz applications. *Sci. Afr.*, e02380. <https://doi.org/10.1016/j.sciaf.2024.e02380>. (2024).
- Mohamed, H. A. et al. Millimeter-wave antenna with gain improvement utilizing reflection FSS for 5G networks. *IEEE Access.* **10**, 73601–73609 (2022).
- Anand, Y. & Nath, V. Gain enhancement of antenna using tuned complementary FSS for wireless communication. *Int. J. Electron.* **112**(6), 1090–1116. <https://doi.org/10.1080/00207217.2024.2354069> (2025).
- Arif, B. et al. A split center resonator FSS based gain enhancement of CPW feed UWB antenna for high gain UWB communication. *IEEE Access.* **12**, 73247–73257. <https://doi.org/10.1109/ACCESS.2024.3403719> (2024).
- Gültekin, S. S. Enhanced gain Dual-Port compact printed meandered Log-Periodic monopole array antenna design with Octagonal-Ring shaped FSS for broadband 28 ghz applications. *Arab. J. Sci. Eng.* **49** (12), 16729–16741 (2024).
- Ali, M., Farman & Bhattacharya, R. Tunable high-gain graphene patch antenna for THz massive MIMO applications using FSS. *Opt. Quant. Electron.* **55** (13), 1204 (2023).
- Khan, I. et al. A compact FSS-based four-port MIMO antenna for low mutual coupling. *IEEE Antennas. Wirel. Propag. Lett.* **22** (12), 2836–2840 (2023).
- Raj, T. et al. A compact quad Port MIMO antenna with gain augmentation using angularly stable and polarization insensitive FSS for 5G communication. *AEU-International J. Electron. Commun.* **190**, 155636 (2025).
- Yang, X., Zhang, L. & Wu, Y. Agile reconfigurable PIN-Diode integrated flexible antenna for Vehicle-to-Everything communications. *IEEE Access.* **11**, 59832–59842 (2023).
- Sufan MA., Hussain N., Abbas A., Lee J., Park SG., Kim N. Mutual coupling reduction of a circularly polarized MIMO antenna using parasitic elements and DGS for V2X communications. *IEEE Access.* **10**, 56388–56400. <https://doi.org/10.1109/ACCESS.2022.3177886> (2022).
- Lee, C. et al. High-Gain Quasi-Omnidirectional dipole array fed by radial power divider for Millimeter-Wave IoT sensing. *IEEE Trans. Antennas Propag.* **72**, 1123–1131 (2024).
- Chen, Y. & Zhou, H. A 4-Port flexible MIMO antenna with isolation enhancement for wireless IoT applications. *Micromachines* **14**, 788 (2023).
- Kumar, A. & Rathi, S. Stub-Loaded compact size Tri-Band antenna for ISM, Sub-6 ghz 5G, and IoT applications. *Int. J. Electron. Commun. (AEÜ)* **163**, 155138 (2024).
- Patel, D. & Sharma, A. Integrated microwave and mm-Wave MIMO antenna module with 360° pattern diversity for 5G internet of things. *Sensors* **23**, 2456 (2023).
- Awan WA., Hussain N., Park SG., Kim N. Intelligent metasurface-based antenna with pattern and beam reconfigurability for Internet of Things applications. *Alexandria Eng J.* **92**, 50–62. <https://doi.org/10.1016/j.aej.2024.02.034> (2024).

41. Said MAM, Misran MH, Othman MAB, Manap RA, Jaafar ASB, Suhaimi S, Hassan NI. Innovation design of high-gain array antenna for 5G communication. *Int J Emerg Technol Adv Eng* **13**(7), 11–20. https://doi.org/10.46338/ijetae0723_02 (2023).

Acknowledgements

The authors extend their appreciation to Northern Border University, Saudi Arabia, for supporting this work through project number (NBU-CRP-2025-2484), also the authors declare that This article has been produced with the financial support of the European Union under the REFRESH – Research Excellence For Region Sustainability and High-tech Industries project number CZ.10.03.01/00/22_003/0000048 via the Operational Programme Just Transition.

Author contributions

Conceptualization, methodology, writing—original draft, results analysis, C.B, I.K. and B.C; data collection, data analysis, writing—review and editing, results analysis, C.B, B.C and A.F; methodology, writing—review and editing, design and presentation, references, C.B and A.F; methodology, writing—review and editing, B.C and H.K; methodology, writing—review and editing, C.B and M.O; methodology, writing—review and editing, B.C and M.O; methodology, writing—review and editing, M.B. All authors have read and agreed to the published version of the manuscript.

Funding

The authors extend their appreciation to Northern Border University, Saudi Arabia, for supporting this work through project number (NBU-CRP-2025-2484).

Institutional Review Board Statement: Not applicable.

Declarations

Competing interests

The authors declare no competing interests.

Additional information

Correspondence and requests for materials should be addressed to C.B.

Reprints and permissions information is available at www.nature.com/reprints.

Publisher's note Springer Nature remains neutral with regard to jurisdictional claims in published maps and institutional affiliations.

Open Access This article is licensed under a Creative Commons Attribution-NonCommercial-NoDerivatives 4.0 International License, which permits any non-commercial use, sharing, distribution and reproduction in any medium or format, as long as you give appropriate credit to the original author(s) and the source, provide a link to the Creative Commons licence, and indicate if you modified the licensed material. You do not have permission under this licence to share adapted material derived from this article or parts of it. The images or other third party material in this article are included in the article's Creative Commons licence, unless indicated otherwise in a credit line to the material. If material is not included in the article's Creative Commons licence and your intended use is not permitted by statutory regulation or exceeds the permitted use, you will need to obtain permission directly from the copyright holder. To view a copy of this licence, visit <http://creativecommons.org/licenses/by-nc-nd/4.0/>.

© The Author(s) 2025